



Computational Investigation of the Effect of Wall Thickness on Rupture Risk in Abdominal Aortic Aneurysms

H. E. Salman^{1,2} and H. C. Yalcin^{1†}

¹ Biomedical Research Center, Qatar University, Doha, P.O. Box 2713, Qatar

² Department of Mechanical Engineering, TOBB University of Economics and Technology, Ankara, Turkey

†Corresponding Author Email: hyalcin@qu.edu.qa

(Received April 19, 2020; accepted September 6, 2020)

ABSTRACT

Cardiovascular disorders are among the most important causes of sudden death and adult disability worldwide. Abdominal aortic aneurysm (AAA) is a critical clinical condition where the aorta dilates beyond 50% of its normal diameter and leads to a risk of rupture. In this study, we performed fluid-structure interaction (FSI) analysis on an eccentric computational AAA model in order to investigate the effects of wall thickness on AAA wall stresses, which are critically important to estimate the rupture risk. For this purpose, we modeled the problem domain using finite element analysis, and coupled the solutions of fluid and structure domains for improving the accuracy of results. ANSYS commercial finite element analysis software was used for modeling, solving, and post-processing the results. Expanded diameter in AAA sac resulted in altered hemodynamics. Wall shear stresses (WSS) caused by the flow are quite low on the AAA sac, which may deteriorate the endothelial cell regeneration and vascular remodeling in the long term. It is concluded that the most critical region for the rupture risk is the posterior distal end of AAA sac due to being exposed to peak mechanical stresses during the cardiac cycle. Obtained results shed light in understanding the rupture risk assessment of AAA.

Keywords: Abdominal aortic aneurysm; Rupture risk assessment; Computational fluid dynamics; Fluid-structure interaction; Finite element analysis; Wall stress.

1. INTRODUCTION

Aorta is the biggest artery in human body which is exposed to large hemodynamic forces. These high mechanical stresses in the arterial structure may result in enlargement of the aortic diameter. Dilatation of the abdominal aorta beyond 50% of its original diameter is known as abdominal aortic aneurysm (AAA) (Scotti *et al.* 2008). The prevalence of AAA is between 0.5–1% of women and 4–8% of men over 50 years of age (Lederle *et al.* 2001; Lederle *et al.* 2000). It is also reported that 1–3% of overall deaths among man between the ages 65–85 in developed countries are caused by AAA (Sakalihan *et al.* 2005). The exact mechanism and etiology of AAA still remain unclear, however, genetic aspects and altered hemodynamics play an important role in the initiation and progression (Salman *et al.* 2019).

AAA may not result in pain and therefore leads to a silent progression, which makes diagnosis challenging at the early stage. The rupture of AAA is

the worst scenario of the disease where 80% of the rupture results in death (Bengtsson and Bergqvist, 1993). The risk assessment of AAA rupture is critical in terms of early detection and repair. However, clinical guidelines that are only based on AAA size and growth rate might lead to insufficient risk assessment, necessitating better predictive approaches.

In AAA, blood flow interacts with the arterial structure and generates fluid shear stresses on the arterial wall. Flow-induced wall shear stresses (WSS) influence the remodeling, inflammation, and degeneration on the arterial wall, since the endothelial cells on the wall are sensitive and reactive to the exerted shear stresses (Franck *et al.* 2013). Mechanical stresses, on the other hand, have a critical effect on the AAA rupture, because the rupture is the failure of the artery due to the applied mechanical forces (Fillinger *et al.* 2003; Wolters *et al.* 2005). Accurate modeling on the AAA wall is a necessity for an accurate rupture risk assessment to understand the critical effects of the wall stresses.

Computational fluid dynamics (CFD) modeling is an important technique for enabling the quantification of the complex flow dynamics within the entire geometry, which is challenging via medical imaging modalities (Soudah *et al.* 2013). In the numerical studies, the flow domain is coupled with the AAA wall due to the interactions between the blood and the arterial wall (Wang and Li, 2013). This approach is known as fluid-structure interaction (FSI) analysis which is a necessity to obtain accurate hemodynamic measures, AAA wall deformations, and associated wall stresses (Scotti *et al.* 2008).

Computational investigations provided important information for rupture mechanics of AAAs. Several different aspects were investigated including the hemodynamics (Bianchi *et al.* 2017; Poelma *et al.* 2015; Tanweer *et al.* 2014; Vorp *et al.* 1998; Wolters *et al.* 2005), AAA diameter (Canchi *et al.* 2018; Fillinger *et al.* 2003), WSS distribution (Arzani and Shadden, 2015; Piccinelli *et al.* 2013; Sugimoto *et al.* 2014), oscillatory shear index (OSI) (Arzani *et al.* 2014), intraluminal thrombus formation (Di Achille *et al.* 2017; Kontopodis *et al.* 2013; Vorp and Geest, 2005), calcification (Speelman *et al.* 2006), local wall thickness (Martufi *et al.* 2009; Raghavan *et al.* 2006; Shang *et al.* 2015), mechanical wall stress (Doyle *et al.* 2014; Ene *et al.* 2014; Kontopodis *et al.* 2014), retrospective analysis of ruptured AAAs (Erhart *et al.* 2015; Qiu *et al.* 2018), wall material models (Simsek and Kwon, 2015), vascular growth and remodeling (Wu and Shadden, 2015), and also the effect of rest and exercise (Khanafar *et al.* 2007; Les *et al.* 2010). During the course of AAA, the thickness of the wall also changes and affects the stresses. Since the rupture is the mechanical failure of the arterial wall, the thickness has great importance to withstand to the dynamic loads. However, the effect of wall thickness in rupture mechanics has not been investigated thoroughly considering the gradual decrease in wall thickness throughout the progression of the disease.

There are many factors affecting the aortic wall thickness. Aging is one of these factors which significantly increases the aortic thickness and stiffness (Pearson *et al.* 1994). Gender is another factor since the women has higher aortic wall thickness than men (Pearson *et al.* 1994). Other factors which influence the wall thickness can be listed as ethnicity, smoking, systolic blood pressure, low density and high density lipoprotein-cholesterol levels, and fasting glucose levels (Rosero *et al.* 2011). In this study, we consider random distribution of these factors by using clinical mean wall thickness values stated in population-based experimental studies.

Experimental studies reported that the range of AAA thickness is within 0.23–4.26 mm, with a median wall thickness of 1.48 mm (Raghavan *et al.* 2006). There is a heterogeneous distribution of wall thickness on AAA, which is a patient-specific parameter and an obscure unknown unless the advanced medical imaging tools are utilized. Due to the challenge in determining the heterogeneous wall thickness field, most of the computational studies employed a uniform wall thickness assumption in the AAA models (Speelman *et al.* 2008;

Venkatasubramaniam *et al.* 2004). When the ruptured AAAs were examined, it was observed that the minimum wall thickness could fall down to 0.23 mm around the rupture site (Raghavan *et al.* 2006).

In this study, we investigated the sole effect of wall thickness on AAA rupture employing a uniform wall thickness model, by gradually reducing the thickness to determine the altered mechanical stresses on the wall. The problem is modeled using FSI approach considering the interaction between the blood and the wall. Wall thickness dependent stresses are elucidated to provide an insight about the rupture risk assessment of AAA.

2. MATERIALS AND METHODS

Two-way FSI approach is employed for modeling the problem domain. In two-way interaction, blood flow leads to deformation on the AAA wall, and the deformed state of the arterial wall alters the geometry of the flow domain. This way, counter-interacting effects between the solid and fluid domains are taken into account. ANSYS Workbench 19.2 (Canonsburg, PA, USA) is used for modeling, solving, post-processing, and coupling the solutions of fluid and solid domains. The system coupling module enables to couple the solutions of both domains. Fluent solver is used for determining the solution of the blood flow. Transient structural module is used for solving the governing equations in the solid domain.

2.1 Model Geometry

A simplified AAA geometry is employed in the model. There is a 10 mm eccentricity between the center of the AAA sac and the aorta centerline, because most of the AAA cases have a certain eccentricity in patient-specific medical images (Les *et al.* 2010). AAA sac is modeled as a sphere with radius of 55 mm. The aortic diameter and total length of AAA model are considered as 25 mm and 180 mm, respectively. In solid domain, three different arterial thicknesses are analyzed for the AAA wall as 0.5 mm, 1 mm, and 1.5 mm. This way, we focused on the pure effect of the wall thickness by elucidating mechanical stresses and arterial deformations to perform the rupture risk assessment of the aneurysm. Normal wall thickness of AAA is modeled as 1.5 mm, similar to the previous computational studies (Doyle *et al.* 2007; Leung *et al.* 2006; Raghavan and Vorp, 2000; Speelman *et al.* 2006; Vorp *et al.* 1998). Since wall thinning is observed around the ruptured regions of AAA (Raghavan *et al.* 2006), the thickness is gradually decreased to 1.0 mm and 0.5 mm for tracking the change in wall stresses depending on the thickness reduction.

2.2 Material Properties and Boundary Conditions

For modeling the flow, blood is modeled as a Newtonian fluid with a mass density of 1060 kg/m³ and viscosity of 0.0035 Pa·s (Simsek and Kwon, 2015; Wang and Li, 2013). AAA wall is modeled as a linearly elastic medium with an elastic modulus of 2.7 MPa, mass density of 2000 kg/m³, and Poisson's ratio of 0.49 (Di Martino *et al.* 2001).

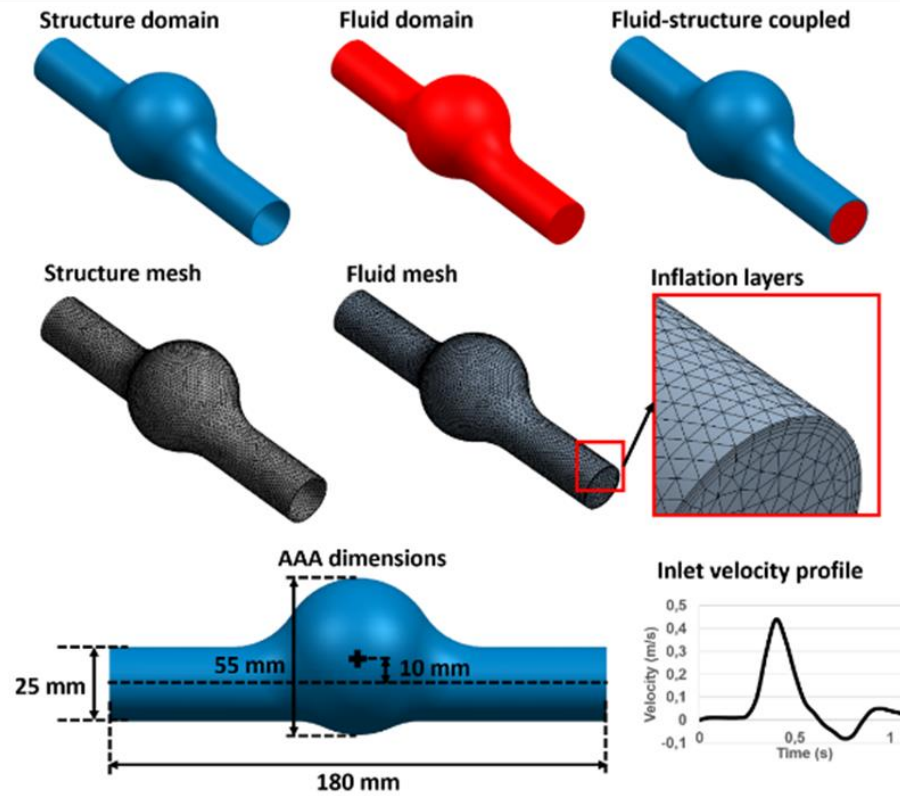


Fig. 1. Fluid and structure geometries and generated meshes. Inflation layers are used on the boundary surfaces of the fluid domain. In the AAA geometry, there is 10 mm eccentricity between the centerline of the AAA sac and aortic centerline. Inlet velocity profile obtained from Scotti *et al.* (2008) is applied at the inlet boundary surface of the fluid model, considering a cardiac cycle with a total time length of 1.1s.

In the fluid domain, the inlet velocity profile given in Fig. 1 is applied at the inlet flow boundary surface (Scotti *et al.* 2008). Zero pressure boundary condition is applied at the outlet surface of the fluid domain. The rest of boundary surfaces in the fluid domain are set as fluid-structure interaction boundaries. At these boundaries, no slip boundary condition is set to guarantee that the flow velocity is zero on the wall.

In the solid domain, two end surfaces of the artery are fixed with zero displacement and zero velocity. Outside surface of the solid domain is a free surface, and the inner surface is a fluid-structure interaction boundary which surrounds the fluid domain.

2.3 Governing Equations

The Navier-Stokes and continuity equations are solved in the fluid domain as provided in Eq. (1) and Eq. (2), respectively (Scotti and Finol, 2007; Zhang *et al.* 2003). In Eq. (1), \mathbf{v} is the fluid velocity vector, \mathbf{w} is the velocity component of the fluid mainly caused by the fluid-structure interaction due to the deformation of solid domain, ρ_f is the fluid mass density, t is time, and $\boldsymbol{\tau}_f$ is the fluid stress tensor. The influence of heat transfer and gravity are neglected due to their insignificant effects on the results.

$$\rho_f \frac{\partial \mathbf{v}}{\partial t} + \rho_f ((\mathbf{v} - \mathbf{w}) \cdot \nabla) \mathbf{v} - \nabla \cdot \boldsymbol{\tau}_f = \mathbf{0} \quad (1)$$

$$\nabla \cdot \mathbf{v} = 0 \quad (2)$$

In Eq. (1), the velocity vector \mathbf{v} defines the flow velocity field for a fixed fluid domain without any deformations on the boundaries. However, the fluid domain deforms in a FSI model. Therefore, a numerical approach is implemented in the fluid domain using arbitrary Lagrangian-Eulerian (ALE) formulation for accounting the deformation of the fluid mesh. For accommodating the velocity change due to the moving boundaries and deformed meshes in a FSI model, the term \mathbf{w} is used for reflecting the moving mesh velocity vector (Scotti and Finol, 2007). This way, the updated velocity vector $(\mathbf{v} - \mathbf{w})$ can be used for the entire domain in the FSI model as given in Eq. (1).

The pressure-based solver is used to solve the set of equations in the fluid domain considering the incompressible nature of the flow. In this solver type, the pressure field is determined using a pressure correction equation by relating the continuity and momentum equations, and the velocity field is determined using the momentum equations (Amindari *et al.* 2017). In the fluid domain, a second order upwind scheme is used for spatial discretization of momentum equations, and a first order upwind scheme is used for the turbulent kinetic energy and turbulent dissipation rate.

The governing equation in solid domain is the

conservation of momentum which is given in Eq. (3) (Scotti *et al.* 2008). In Eq. (3), $\boldsymbol{\tau}_s$ is the solid stress tensor, ρ_s is the mass density of solid, and \mathbf{a}_s is the acceleration vector in the solid domain.

$$\nabla \cdot \boldsymbol{\tau}_s = \rho_s \mathbf{a}_s \quad (3)$$

Mechanical stress on the wall is the main parameter for the rupture risk assessment. Therefore, von-Mises stresses are calculated on the arterial wall using the principal stresses to predict the occurrence of failure as given in Eq. (4) (Scotti *et al.* 2008).

$$\frac{1}{2} [(\sigma_1 - \sigma_2)^2 + (\sigma_2 - \sigma_3)^2 + (\sigma_3 - \sigma_1)^2] > \sigma_F^2 \quad (4)$$

In Eq. (4), von-Mises stress is equal to the square root of the terms written at the left side. The uniaxial failure strength is defined by σ_F , and the principal stresses are defined by σ_1 , σ_2 , and σ_3 . In order to prevent the mechanical failure of the arterial wall, the square of von-Mises stress must be greater than the square of σ_F .

2.4 Mesh Independence

Mesh independent results are obtained by comparing the results of three meshes with different mesh densities. Coarse, moderate, and dense meshes are composed of 58.436, 187.228, and 528.229 tetrahedral elements in the fluid domain, and 14.597, 33.111, and 67.877 tetrahedral elements in the solid domain, respectively. Volume averaged vorticity magnitudes within one cardiac cycle in the fluid domain are determined with 3.45% difference between the coarse and moderate meshes. This difference is determined as 1.98% between the moderate and dense meshes. Considering these differences, the results of the moderate mesh is accepted as accurate due to having a difference less than 3% compared to the dense mesh results (Kelsey *et al.* 2017). The moderate mesh is used for further presented results. In order to increase the solution accuracy, inflation layers are used on the FSI boundaries of the fluid mesh. Three full cardiac cycles were run and the last cardiac cycle is used for the numerical analysis. This way, transient effects in the first two cardiac cycles are eliminated to achieve accurate results. For the wall thickness of 1 mm, we compared the average wall deformation at different cardiac cycles. The average wall deformation difference between the first and second cardiac cycles is calculated as 16.1%. This difference is decreased to 3.0% between the second and third cardiac cycles, showing that the transient effects are significantly eliminated in the last cardiac cycle.

3. RESULTS AND DISCUSSION

Results are investigated in separate sections considering the fluid and solid domains. In the fluid domain, alterations in hemodynamic parameters such as pressure, flow velocity, and WSS are analyzed. In the solid domain, mechanical stresses and structural deformations are the main interest.

3.1 Fluid Domain Results

The full length of one cardiac cycle is 1.1s. We mainly investigated five time points at 0.2s, 0.45s, 0.6s, 0.8s, and 1.0s in order to clearly observe the changes at systolic and diastolic phases. For all different wall thicknesses, the fluid domain has nearly the same geometrical dimensions, and therefore almost the same results are achieved in the fluid domain due to the limited deformation of the AAA wall. In Fig. 2, the velocity and pressure profiles are compared to observe the similarity of flow patterns for different AAA wall thicknesses. The flow results are compared at 0.5s, since high speed flow is observed at the proximal side of AAA at that instant. It is seen that the recirculating vortices are in the same spatial locations for all wall thicknesses and also the pressure distributions are in well agreement. This similarity of flow conditions is due to the limited deformation of the wall depending on the thickness. In Fig. 3 and Fig. 4, 2D and 3D flow velocity streamlines are presented respectively for the wall thickness of 1 mm.

In Fig. 3, the streamlines are presented on the longitudinal cross-sectional plane of the fluid domain for the ease of comparison. Peak flow velocities are observed at 0.45s, which is the instant of the peak systole. After observing the peak values, the velocities gradually decrease until the end of the diastolic phase. The turbulent flow characteristics are mostly apparent at the diastolic phase which can be clearly seen at the instants of 0.60s, 0.80s, and 1.00s. At these instants, the recirculating vortex in the AAA sac is clearly visible. The rotational speed of the vortex remains similar at instants of 0.6s and 0.8s. The rotational speed decreases at the end of the diastolic phase at 1.00s. There is no circulatory behavior at the systolic phase. The peak flow velocity reaches approximately 0.5 m/s.

In Fig. 5, the pressure contours are presented on the longitudinal cross-sectional plane. The pressure gradient which is the difference between the inlet and outlet of AAA has its maximum value at the instant of 0.45s. The maximum pressure gradient is around 200 Pa. The highest pressure in AAA sac is observed at 0.60s where its value is around 100 Pa. The pressure distributions are relatively uniform at the instants of 0.2s and 0.8s.

In Fig. 6, WSS contours are presented on the AAA wall. These shear stresses are critical since they regulate the remodeling and adaption of the endothelial cells on the arterial wall. Low shear stresses and oscillating shear behavior are the factors which deteriorate the regular cellular mechanisms. AAA sac is exposed to relatively lower WSS (lower than 1.0 Pa) within the entire cardiac cycle. This is mainly due to the sudden enlargement of the flow volume in the sac, leading to reduced flow velocities. WSS values on the proximal and distal ends of AAA sac have high temporal variability. The maximum WSS reaches approximately 2.0 Pa on the proximal end at 0.45s, and on the distal end at 0.60s. Spatial distribution of WSS is heterogeneous, particularly at 0.45s, in which the systolic flow is observed.

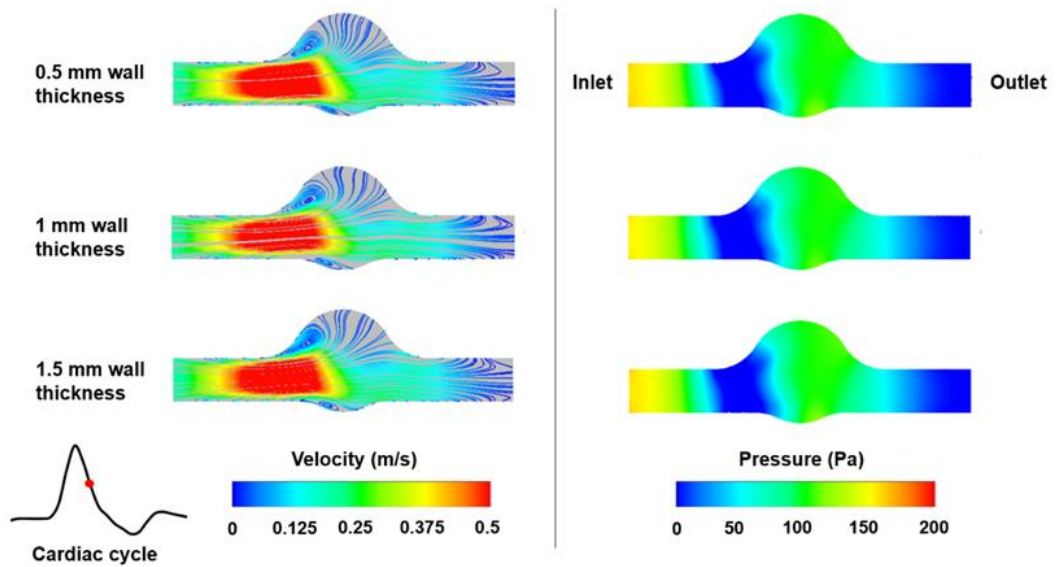


Fig. 2. Comparison of streamlines and pressure distributions for different wall thicknesses at 0.5s. Results are provided on the longitudinal cross-sectional plane. Flow is from left to right.

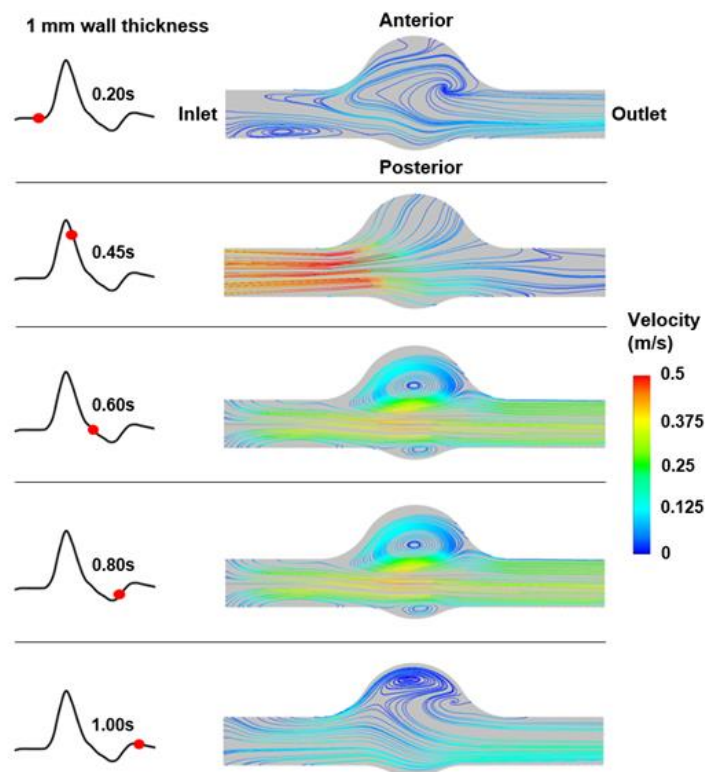


Fig. 3. 2D flow velocity streamlines shown on the longitudinal cross-sectional plane for 1 mm thickness model. Flow is from left to right. The top and bottom of each contour plot are the anterior and posterior sides, respectively. The instant within the cardiac cycle is shown at left side of the contour plots.

For the selected points provided in Fig. 6, the temporal changes in WSS are analyzed to determine the variability of the shear stress amplitudes within

the cardiac cycle. In Table 1, WSS values on the selected points are given at various instants. WSS values are measured on 10 different points

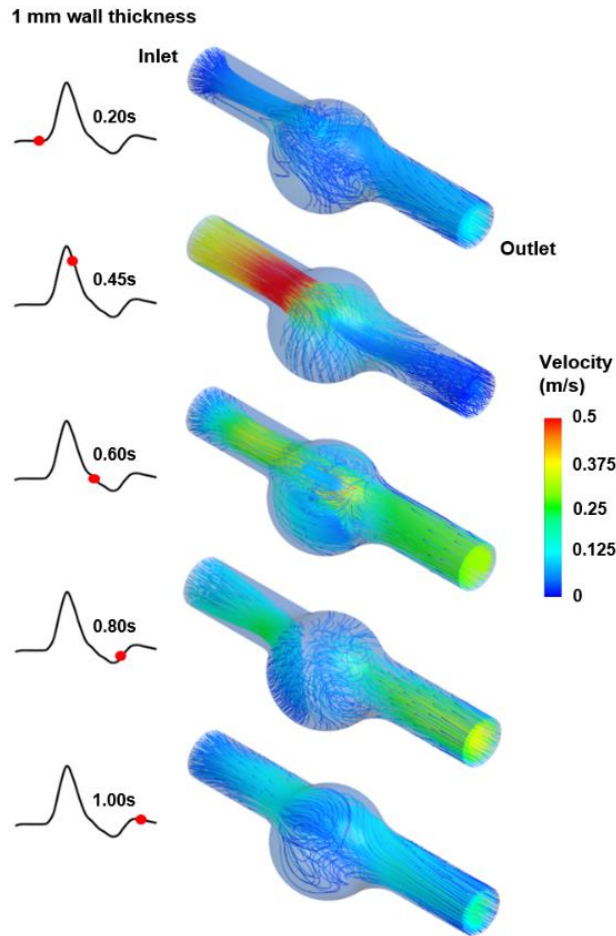


Fig. 4. 3D flow velocity streamlines at different instants of cardiac cycle for 1 mm wall thickness model. The instants are shown at the left side of the contour plots.

Table 1 WSS values and standard deviations on the selected points provided in Fig. 6

WSS (Pa)	0s	0.2s	0.45s	0.6s	0.8s	1.0s	Standard Deviation
Point 1	0.411	0.684	1.716	0.388	1.543	0.368	0.615
Point 2	0.419	0.933	0.381	2.002	0.825	0.968	0.587
Point 3	0.194	0.026	0.665	0.324	0.034	0.141	0.239
Point 4	0.258	0.088	0.627	1.269	0.237	0.442	0.425
Point 5	0.084	0.144	0.228	1.663	0.443	0.120	0.609
Point 6	0.414	0.691	1.816	0.456	1.380	0.482	0.585
Point 7	0.218	0.417	1.925	0.146	0.326	1.049	0.689
Point 8	0.516	0.017	1.451	1.000	0.045	0.470	0.557
Point 9	1.190	0.209	1.829	2.048	0.458	1.053	0.726
Point 10	0.481	0.328	0.055	1.870	0.588	0.386	0.639

distributed on the anterior and posterior sides of the AAA. The standard deviations are calculated using 6 different time points given in Table 1 and the minimum standard deviation is determined for point 3 which is placed on the anterior side of the AAA sac as shown in Fig. 6. This indicates that the variation of WSS values are limited on the mostly enlarged side of the AAA. For most of the cases, AAA sac

expands towards the anterior side, and therefore WSS values are relatively stable on the anterior side of the AAA sac when compared to the points on the posterior side. For a more comprehensive investigation on temporal WSS variability, OSI can be calculated for mapping the oscillatory behavior of shear stress amplitudes as a function of time as given in Eq. (5).

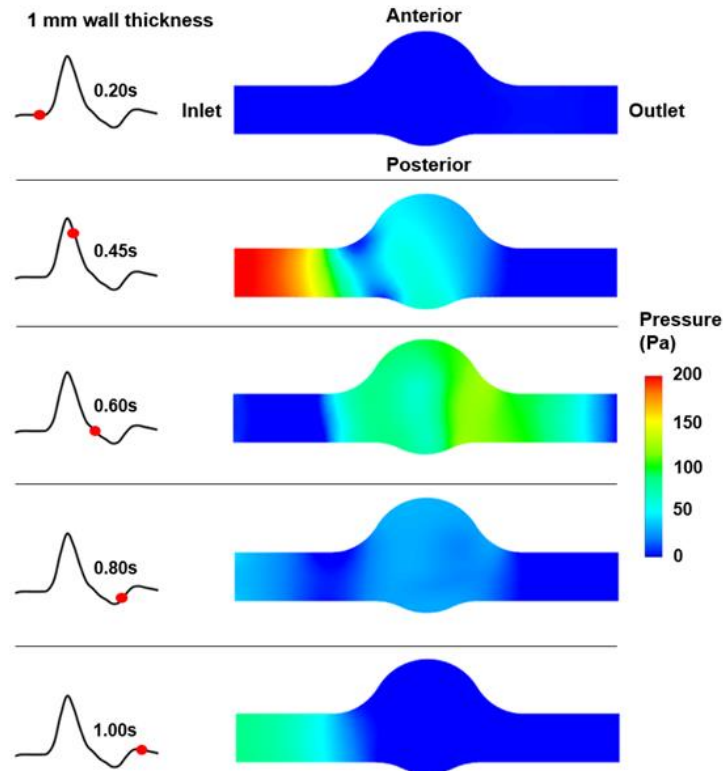


Fig. 5. Pressure contours shown on the longitudinal cross-sectional plane for 1 mm wall thickness. Flow is from left to right. Anterior side is at the top and posterior side is at the bottom of the contour plots.

$$OSI = \frac{1}{2} \left(1 - \frac{\frac{1}{T} \int_{t-T}^t WSS dt}{\frac{1}{T} \int_{t-T}^t |WSS| dt} \right) \quad (5)$$

3.2 Solid Domain Results

In the solid domain, total deformations and von-Mises stresses are investigated for three different AAA wall thicknesses. In Fig. 7, Fig. 8, and Fig. 9, the results are provided for wall thicknesses of 0.5 mm, 1.0 mm, and 1.5 mm, respectively. The spatial distributions of von-Mises stresses are similar for three wall thicknesses. AAA sac experiences limited stress, however, the distal and proximal ends of AAA are exposed to relatively higher von-Mises stresses. There is a ring-shaped high stress region at the distal and proximal ends of AAA, particularly at the instants of 0.6s and 0.8s. The inlet side of the model is exposed to relatively higher stresses and deformations. The instants and values of peak total deformation and peak equivalent von-Mises stress are given at the bottom of each figure.

Increased AAA wall thickness resulted in enhanced wall strength, which is reducing the total deformation on the AAA wall. The reduced deformations lead to less severe stresses on the wall. This effect can be observed in Fig. 10, where the total deformations and von-Mises stresses are presented by calculating the average values within the entire AAA wall. According to the results, there are two peak values within 0.4–0.6s similar to a spring motion, which is considered to be related with the peak flow velocity observed around 0.4s. Then, a

relatively lower third peak is observed around 1.0s, depending on the slight increase in the flow velocity profile around 0.9s.

As presented in Fig. 10(c), the maximum deformations are determined as 0.315 mm, 0.117 mm, and 0.071 mm for the wall thicknesses of 0.5 mm, 1.0 mm, and 1.5 mm, respectively. The maximum deformations increased by 63.7% when the thickness decreased from 1.5 mm to 1.0 mm. The maximum deformations increased by 169.8%, when the wall thickness is reduced from 1.0 mm to 0.5 mm. This shows that as the thickness decreases, more pronounced deformations are observed on the wall, indicating a nonlinear increase in wall deformations depending on the thickness reduction. In Fig. 11, the maximum deformed states are presented for different wall thicknesses. For the maximum deformed state, AAA sac tends to move towards the anterior side. This movement becomes more prominent as the wall thickness decreases.

As provided in Fig. 10(d), the maximum von-Mises stresses on the AAA wall are measured as 0.00907 MPa, 0.00510 MPa, and 0.00345 MPa for 0.5 mm, 1.0 mm, and 1.5 mm wall thicknesses, respectively. The relative difference in peak von-Mises stresses between 0.5 mm and 1.0 mm wall thickness is 77.74%, and the difference between 1.0 mm and 1.5 mm thickness is 48.02%. When the increase in stress levels are examined, it is seen that there is an almost linear relationship between the wall thickness and the associated von-Mises stresses, opposing to the

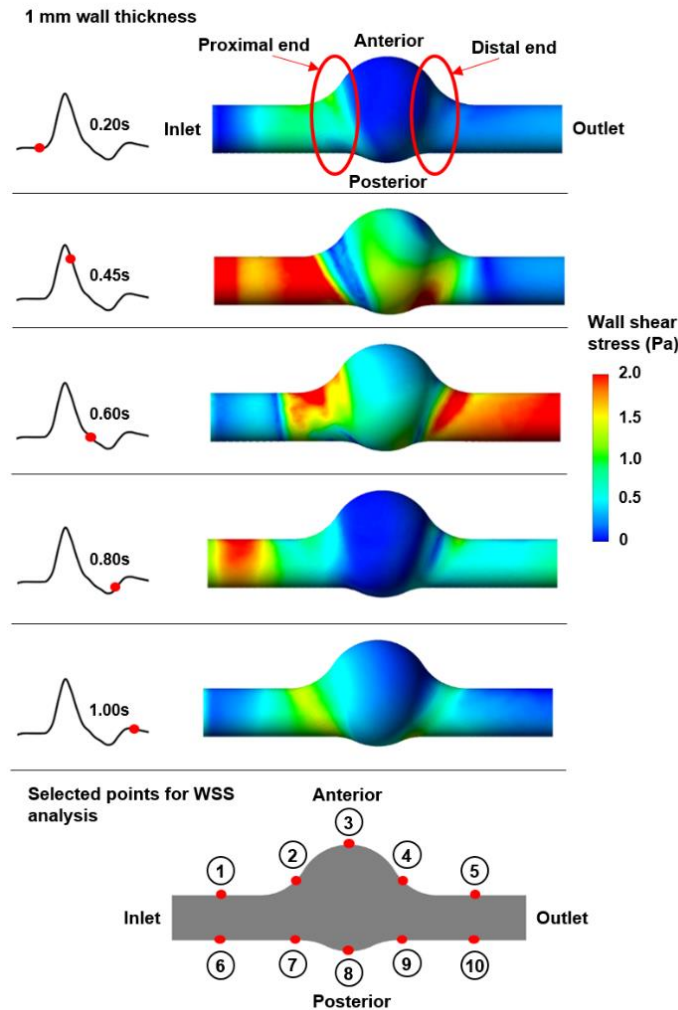


Fig. 6. Wall shear stress (WSS) contours shown on the AAA wall for 1 mm wall thickness. Flow is from left to right. Proximal and distal ends of AAA are shown in ellipses. Anterior side is at the top and posterior side is at the bottom of the contour plots. WSS values are analyzed for the selected points provided at the bottom of the figure.

nonlinear relationship between the deformation and wall thickness. Von-Mises stresses proportionally increase on the wall depending on the wall thickness reduction. Almost three times increased peak stress is measured when the wall thickness is reduced from 1.5 mm to 0.5 mm. Three times reduction in wall thickness resulted in almost three times increased peak von-Mises stress. Peak mechanical stress is the most important factor for the rupture, since it is directly related to the mechanical failure of the AAA wall.

The minimum and maximum von-Mises stresses are presented in Fig. 12 for different AAA wall thicknesses. The amplitude range of minimum mechanical stresses are comparable for all different wall thicknesses. However, the instants of the peaks of minimum stresses show a difference. When the maximum von-Mises stresses are investigated as a function of time, the amplitude levels of maximum mechanical stresses are clearly distinguishable for different wall thicknesses. Opposing to the behavior

of the minimum stresses, the instants of the peaks of the maximum stresses are similar for all different AAA wall thicknesses.

Relative differences between the maximum values are also verified using the average results presented in Fig. 10. Using the average deformations considering the entire wall during one cardiac cycle, it is found that the average AAA deformation is increased by 141.92% when the wall thickness is reduced from 1.0 mm to 0.5 mm. If the wall thickness is reduced from 1.5 mm to 1.0 mm, the average deformation is increased by 55.89%. Similar results are also determined for the average von-Mises stresses. The average von-Mises stress is increased by 110.66% when the wall thickness is decreased from 1.0 mm to 0.5 mm. This increase is calculated as 46.29% when the wall thickness is decreased from 1.5 mm to 1.0 mm.

Both the deformation and von-Mises stress contours represent a spatially nonhomogeneous behavior, showing the complicated stress patterns on the AAA

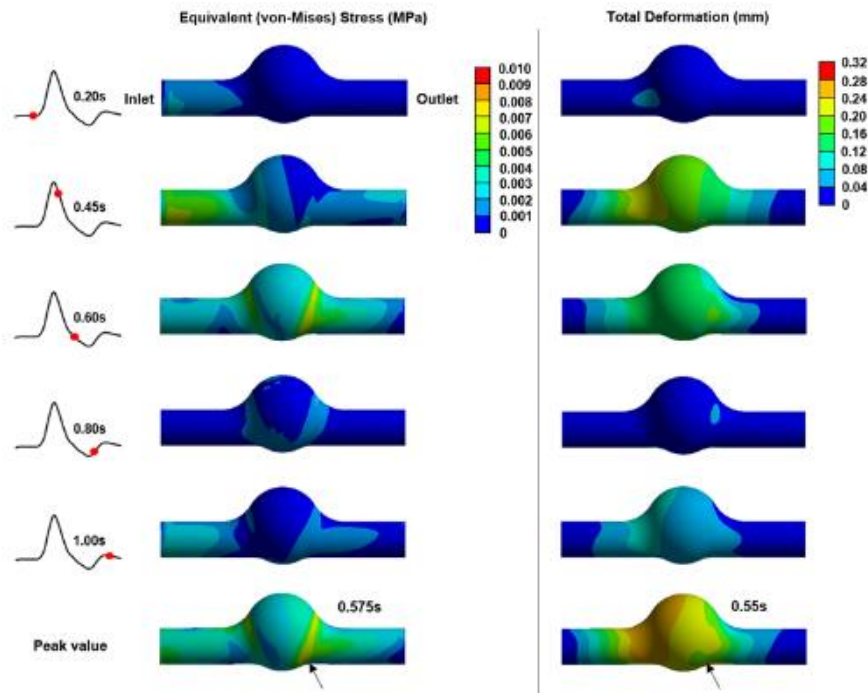


Fig. 7. Equivalent von-Mises stress and total deformation contours on the outside surface of solid domain for wall thickness of 0.5 mm. Inlet is at the left and outlet is at the right side. Anterior side is at the top and posterior side is at the bottom of the contour plots. Locations of peak values are shown by arrows. The instants of the peak deformation and peak von-Mises stress are given on the contour plots.

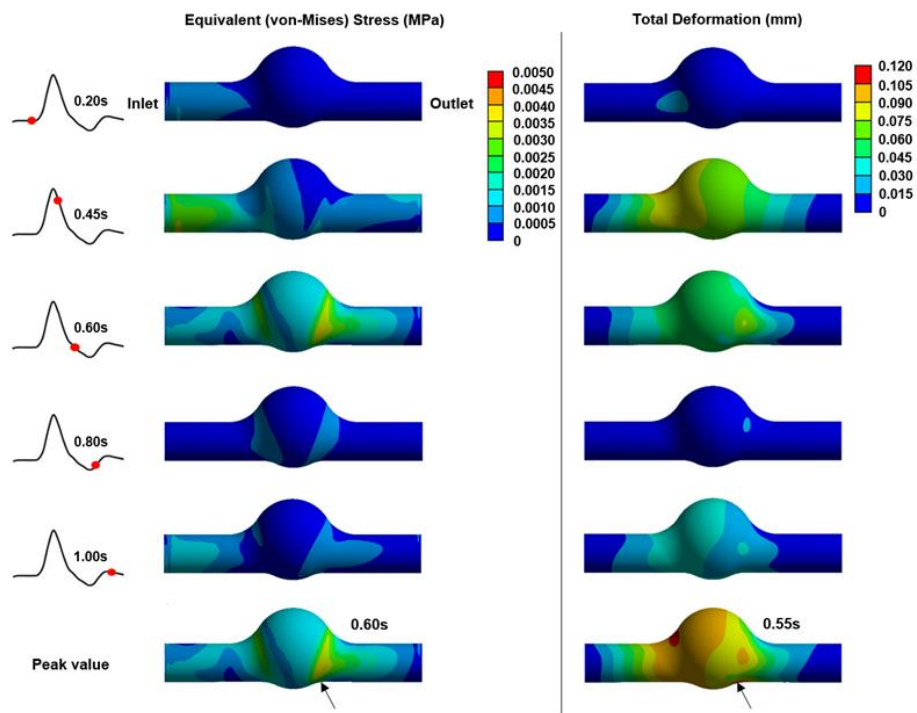


Fig. 8. Equivalent von-Mises stress and total deformation contours on the outside surface of solid domain for wall thickness of 1.0 mm. Inlet is at the left and outlet is at the right side. Anterior side is at the top and posterior side is the bottom of the contour plots. Locations of peak values are shown by arrows. The instants of the peak deformation and peak von-Mises stress are given on the contour plots.

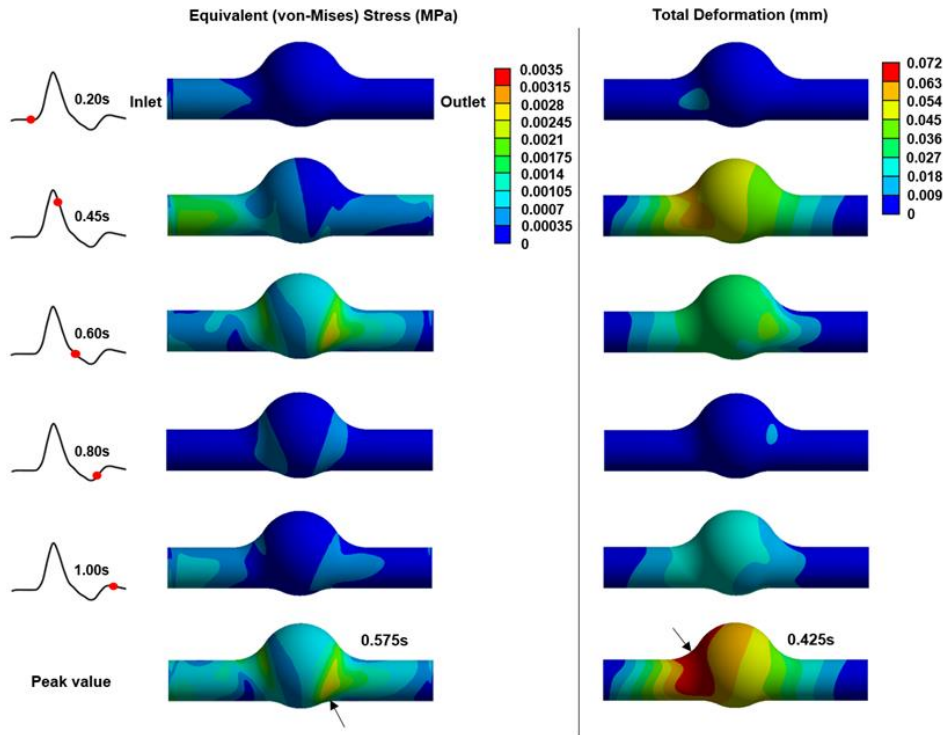


Fig. 9. Equivalent von-Mises stress and total deformation contours on the outside surface of solid domain for wall thickness of 1.5 mm. Inlet is at the left and outlet is at the right side. Anterior side is the top and posterior side is the bottom of the contour plots. Locations of peak values are shown by arrows. The instants of the peak deformation and peak von-Mises stress are given on the contour plots.

wall. However, the critical regions are found at the distal and proximal ends of the AAA for all different cases. This is indicating that these regions are prone to rupture due to the mechanical stresses exerted on the wall. The deformation and von-Mises stress patterns represent similar behavior, because the increased deformation leads to excessive mechanical stresses. The maximum stresses are determined at the posterior distal end of AAA for all different wall thicknesses. These findings suggest that the posterior distal end is a critical region for the rupture risk assessment.

For wall thicknesses of 0.5 mm and 1.0 mm, the locations of peak deformation and peak mechanical stress are almost the same. On the other hand, for the wall thickness of 1.5 mm, the location of peak deformation is on the anterior proximal end of AAA, which is different from the location of the peak mechanical stress.

There is a time lag between the instants of peak values of deformation and von-Mises stress as presented in Fig. 7, Fig. 8, and Fig. 9. For all models, the instant of peak stress is observed after the moment of peak deformation. However, the time lag between the peak deformation and peak stress increases with the increasing AAA wall thickness. For 0.5 mm, peak deformation is observed at 0.55s and peak mechanical stress is observed at 0.575s, implying a difference of 0.025s in between. For the wall thickness of 1.0 mm, peak deformation is again seen at 0.55s, however, peak stress is observed at

0.60s, demonstrating a time difference of 0.05s. For the wall thickness of 1.5 mm, which represents a healthier case, this time difference is increased to 0.15s, since the peak deformation is seen at 0.425s and the peak stress is observed at 0.575s. The time range of 0.575–0.6s corresponds to early diastole and it is found critical because AAA wall is exposed to the peak mechanical stresses within this time period. It is understood that the reduced time lag for smaller wall thickness results in observing the peak deformation and peak wall stress approximately at the same time, which may also be critical and increase the possible arterial damage. This result suggests that healthy thicker wall experience mechanical stresses in an extended period which enables to spread the effect of stress over time, and which might help to withstand stress. On the other hand, thinner vessels are exposed to higher stresses within a much shorter period of time, which is increasing the risk of mechanical failure.

There are some limitations in our study. The wall thickness is modeled as uniform, however, there may be a heterogeneous thickness pattern on the AAA wall, which may locally increase the stresses (Raghavan *et al.* 2004). The heterogeneous wall thickness on the wall should be analyzed in detail utilizing patient-specific medical imaging, especially around the distal and proximal ends of the AAA sac. Because, any localized decrease in the wall thickness on AAA can exaggerate the mechanical stress, and consequently increase the risk of AAA rupture. FSI

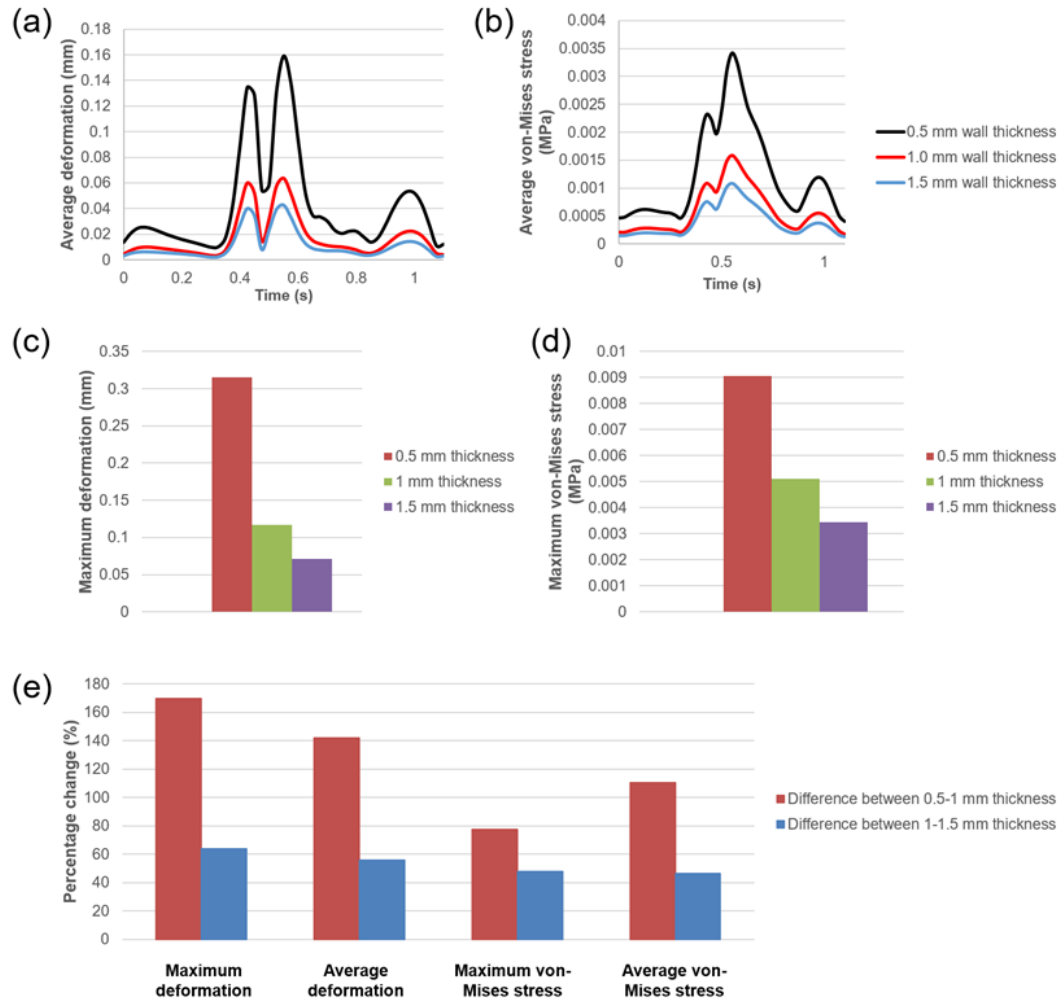


Fig. 10. Deformations and equivalent von-Mises stresses. (a) Average deformation for different wall thicknesses. (b) Average von-Mises (mechanical) stresses for different wall thicknesses. (c) Maximum deformation. (d) Maximum von-Mises stress. (e) Percentage change in maximum deformation and maximum von-Mises stress between 0.5 mm – 1 mm wall thicknesses and between 1 mm – 1.5 mm wall thicknesses.

simulations of patient-specific models would provide more detailed information (Chandra *et al.* 2013). The wall is considered as a single layered structure. This approach can be improved by introducing multiple structural layers on the AAA wall (Humphrey and Holzapfel, 2012; Lasheras, 2006). Another limitation is the linear elastic modeling of the wall structural behavior. In reality, AAA wall may have hyperelastic and viscoelastic material properties (Vande Geest *et al.* 2006a; Vande Geest *et al.* 2006b). Consideration of these parameters would enhance the accuracy of the structural deformations and associated mechanical stresses. In the fluid domain, the blood can be modeled as a non-Newtonian fluid with varying viscosity depending on the shear rate (Khanafar *et al.* 2006; Thurston, 1979). Considering the aforementioned improvements, the hemodynamic parameters can be estimated more accurately. However, we believe that the main conclusions

drawn in this investigation would not change in terms of the sole effect of the wall thickness.

In this study, important findings are obtained in the computational comparison of different AAA wall thicknesses. According to the flow analysis, proximal and distal ends of AAA are critical due to being exposed to highly dynamic WSS environment. In addition, AAA sac experiences relatively much smaller WSS, which is negatively affecting the remodeling of the arterial wall and also increasing the risk of intraluminal thrombus formation. The change in wall thickness did not affect the flow behavior, but it significantly altered the wall deformations and mechanical stresses. According to the FSI results, highest mechanical stresses are observed at the posterior distal end of AAA. For the mechanical stresses, three peak values are observed within the cardiac cycle. The first two peak stresses are related to the peak inlet flow velocity, and the third peak value is associated with a relative increase

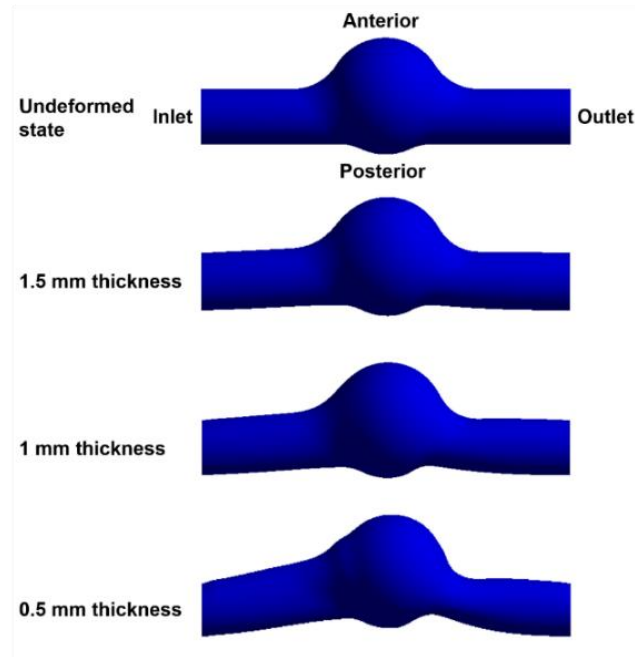


Fig. 11. Maximum deformed state for different AAA wall thicknesses. The deformed states represent 40-times exaggerated deformations.

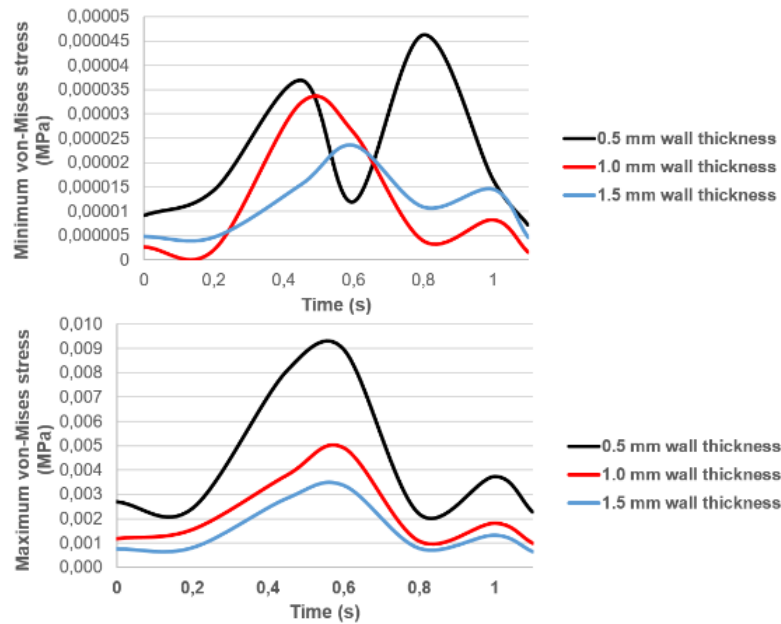


Fig. 12. Minimum and maximum von-Mises stresses considering different AAA wall thicknesses.

in the flow rate towards the end of the cardiac cycle. It is stated that posterior region of AAA may have slightly lower wall thicknesses (Raghavan *et al.* 2006), which is increasing the risk of rupture. Therefore, the local wall thinning effect should be taken into account, since it significantly changes the mechanical stresses.

4. CONCLUSION

We analyzed a simplified AAA model to focus on the direct effects of AAA wall thickness on the risk of rupture. According to our analysis, the posterior distal end of AAA is more prone to rupture, regardless of the wall thickness. Hemodynamic parameters such as WSS have a long-term effect on the development and progression of the aortic

dilation. On the other hand, mechanical parameters such as von-Mises stresses on the wall have critical role in sudden rupture and should be prioritized during developing an early diagnosis modality that can determine the rupture risk of the patient-specific AAA.

ACKNOWLEDGEMENTS

This study is funded by Qatar University International Research Collaboration Co-Funds (IRCC) Program (IRCC 2020-002) and Qatar National Research Fund (QNRF), National Priority Research Program (NPRP 10-0123-170222).

CONFLICTS OF INTEREST

No conflict of interest was declared by the authors.

REFERENCES

- Amindari, A., L. Saltik, K. Kirkkopru, M. Yacoub and H. C. Yalcin (2017). Assessment of calcified aortic valve leaflet deformations and blood flow dynamics using fluid-structure interaction modeling. *Informatics in Medicine Unlocked* 9, 191-199.
- Arzani, A. and S. C. Shadden (2015). Characterizations and correlations of wall shear stress in aneurysmal flow. *Journal of Biomechanical Engineering* 138(1), 0145031-01450310.
- Arzani, A., G. Y. Suh, R. L. Dalman and S. C. Shadden (2014). A longitudinal comparison of hemodynamics and intraluminal thrombus deposition in abdominal aortic aneurysms. *American Journal of Physiology-Heart and Circulatory Physiology* 307(12), H1786-H1795.
- Bengtsson, H. and D. Bergqvist (1993). Ruptured abdominal aortic aneurysm: A population-based study. *Journal of Vascular Surgery* 18(1), 74-80.
- Bharadwaj, K. N., C. Spitz, A. Shekhar, H. C. Yalcin and J. T. Butcher (2012). Computational fluid dynamics of developing avian outflow tract heart valves. *Annals of Biomedical Engineering* 40(10), 2212-2227.
- Bianchi, D., E. Monaldo, A. Gizzi, M. Marino, S. Filippi and G. Vairo (2017). A FSI computational framework for vascular physiopathology: A novel flow-tissue multiscale strategy. *Medical Engineering & Physics* 47, 25-37.
- Canchi, T., A. Saxena, E. Y. K. Ng, E. C. H. Pwee and S. Narayanan (2018). Application of fluid-structure interaction methods to estimate the mechanics of rupture in asian abdominal aortic aneurysms. *Bionanoscience* 8(4), 1035-1044.
- Chandra, S., S. S. Raut, A. Jana, R. W. Biederman, M. Doyle, S. C. Muluk and E. A. Finol (2013). Fluid-structure interaction modeling of abdominal aortic aneurysms: the impact of patient-specific inflow conditions and fluid/solid coupling. *Journal of Biomechanical Engineering* 135(8), 0810011-08100114.
- Di Achille, P., G. Tellides and J. D. Humphrey (2017). Hemodynamics-driven deposition of intraluminal thrombus in abdominal aortic aneurysms. *International Journal for Numerical Methods in Biomedical Engineering* 33(5), e2828.
- Di Martino, E. S., G. Guadagni, A. Fumero, G. Ballerini, R. Spirito, P. Biglioli and A. Redaelli (2001). Fluid-structure interaction within realistic three-dimensional models of the aneurysmatic aorta as a guidance to assess the risk of rupture of the aneurysm. *Medical Engineering & Physics* 23(9), 647-655.
- Doyle, B. J., A. Callanan and T. M. McGloughlin (2007). A comparison of modelling techniques for computing wall stress in abdominal aortic aneurysms. *Biomedical Engineering Online* 6(1), 38.
- Doyle, B. J., T. M. McGloughlin, K. Miller, J. T. Powell and P. E. Norman (2014). Regions of high wall stress can predict the future location of rupture of abdominal aortic aneurysm. *Cardiovascular and Interventional Radiology* 37(3), 815-818.
- Ene, F., P. Delassus and L. Morris (2014). The influence of computational assumptions on analysing abdominal aortic aneurysm haemodynamics. *Proceedings of the Institution of Mechanical Engineers, Part H: Journal of Engineering in Medicine* 228(8), 768-780.
- Erhart, P., A. Hyhlik-Durr, P. Geisbusch, D. Kotelits, M. Muller-Eschner, T. C. Gasser, H. von Tengg-Kobligh and D. Bockler (2015). Finite element analysis in asymptomatic, symptomatic, and ruptured abdominal aortic aneurysms: In search of new rupture risk predictors. *European Journal of Vascular and Endovascular Surgery* 49(3), 239-245.
- Fillinger, M. F., S. P. Marra, M. L. Raghavan and F. E. Kennedy (2003). Prediction of rupture risk in abdominal aortic aneurysm during observation: Wall stress versus diameter. *Journal of Vascular Surgery* 37(4), 724-732.
- Franck, G., J. Dai, A. Fifre, S. Ngo, C. Justine, S. Michineau, E. Allaire and M. Gervais (2013). Reestablishment of the endothelial lining by endothelial cell therapy stabilizes experimental abdominal aortic aneurysms. *Circulation* 127(18), 1877-1887.
- Humphrey, J. D. and G. A. Holzapfel (2012). Mechanics, mechanobiology, and modeling of human abdominal aorta and aneurysms. *Journal of Biomechanics* 45(5), 805-814.
- Kelsey, L. J., J. T. Powell, P. E. Norman, K. Miller and B. J. Doyle (2017). A comparison of hemodynamic metrics and intraluminal

- thrombus burden in a common iliac artery aneurysm. *International Journal for Numerical Methods in Biomedical Engineering* 33(5), e2821.
- Khanafer, K. M., J. L. Bull, G. R. Upchurch and R. Berguer (2007). Turbulence significantly increases pressure and fluid shear stress in an aortic aneurysm model under resting and exercise flow conditions. *Annals of Vascular Surgery* 21(1), 67-74.
- Khanafer, K. M., P. Gadhoke, R. Berguer and J. L. Bull (2006). Modeling pulsatile flow in aortic aneurysms: effect of non-Newtonian properties of blood. *Biorheology* 43(5), 661-679.
- Kontopodis, N., E. Metaxa, Y. Papaharilaou, E. Georgakarakos, D. Tsetis and C. V. Ioannou (2013). Changes in geometric configuration and biomechanical parameters of a rapidly growing abdominal aortic aneurysm may provide insight in aneurysms natural history and rupture risk. *Theoretical Biology and Medical Modelling* 10(1), 67.
- Kontopodis, N., E. Metaxa, Y. Papaharilaou, E. Tavlas, D. Tsetis and C. Ioannou (2014). Advancements in identifying biomechanical determinants for abdominal aortic aneurysm rupture. *Vascular* 23(1), 65-77.
- Lasheras, J. C. (2007). The biomechanics of arterial aneurysms. *Annual Review of Fluid Mechanics* 39, 293-319.
- Lederle, F. A., G. R. Johnson and S. E. Wilson (2001). Abdominal aortic aneurysm in women. *Journal of Vascular Surgery* 34(1), 122-126.
- Lederle, F. A., G. R. Johnson, S. E. Wilson, E. P. Chute, R. J. Hye, M. S. Makaroun, G. W. Barone, D. Bandyk, G. L. Moneta and R. G. Makhoul (2000). The aneurysm detection and management study screening program: Validation cohort and final results. *Archives of Internal Medicine* 160(10), 1425-1430.
- Les, A. S., S. C. Shadden, C. A. Figueroa, J. M. Park, M. M. Tedesco, R. J. Hefkens, R. L. Dalman and C. A. Taylor (2010). Quantification of hemodynamics in abdominal aortic aneurysms during rest and exercise using magnetic resonance imaging and computational fluid dynamics. *Annals of Biomedical Engineering* 38(4), 1288-1313.
- Leung, J. H., A. R. Wright, N. Cheshire, J. Crane, S. A. Thom, A. D. Hughes and Y. Xu (2006). Fluid structure interaction of patient specific abdominal aortic aneurysms: a comparison with solid stress models. *Biomedical Engineering Online* 5(1), 33.
- Martufi, G., E. S. Di Martino, C. H. Amon, S. C. Muluk and E. A. Finol (2009). Three-dimensional geometrical characterization of abdominal aortic aneurysms: Image-based wall thickness distribution. *Journal of Biomechanical Engineering* 131(6), 061015.
- Olcay, A. B., A. Amindari, K. Kirkkopru and H. C. Yalcin (2018). Characterization of disturbed hemodynamics due to stenosed aortic jets with a Lagrangian Coherent structures technique. *Journal of Applied Fluid Mechanics* 11, 375-384.
- Pearson, A. C., R. Guo, D. A. Orsinelli, P. F. Binkley and T. J. Pasierski (1994). Transesophageal echocardiographic assessment of the effects of age, gender, and hypertension on thoracic aortic wall size, thickness, and stiffness. *American Heart Journal* 128(2), 344-351.
- Piccinelli, M., C. Vergara, L. Antiga, L. Forzenigo, P. Biondetti and M. Domanin (2013). Impact of hemodynamics on lumen boundary displacements in abdominal aortic aneurysms by means of dynamic computed tomography and computational fluid dynamics. *Biomechanics and Modeling in Mechanobiology* 12(6), 1263-1276.
- Poelma, C., P. N. Watton and Y. Ventikos (2015). Transitional flow in aneurysms and the computation of haemodynamic parameters. *Journal of The Royal Society Interface* 12(105), 20141394.
- Qiu, Y., D. Yuan, J. Wen, Y. Fan and T. Zheng (2018). Numerical identification of the rupture locations in patient-specific abdominal aortic aneurysms using hemodynamic parameters. *Computer Methods in Biomechanics and Biomedical Engineering* 21(1), 1-12.
- Raghavan, M. L. and D. A. Vorp (2000). Toward a biomechanical tool to evaluate rupture potential of abdominal aortic aneurysm: identification of a finite strain constitutive model and evaluation of its applicability. *Journal of Biomechanics* 33(4), 475-482.
- Raghavan, M. L., J. Kratzberg, E. M. C. de Tolosa, M. M. Hanaoka, P. Walker and E. S. da Silva (2006). Regional distribution of wall thickness and failure properties of human abdominal aortic aneurysm. *Journal of Biomechanics* 39(16), 3010-3016.
- Raghavan, M., J. Kratzberg and E. S. da Silva (2004). Heterogeneous, variable wall-thickness modeling of a ruptured abdominal aortic aneurysm. *ASME 2004 International Mechanical Engineering Congress and Exposition*, 271-272.
- Rosero, E. B., R. M. Peshock, A. Khera, P. Claggett, H. Lo and C. H. Timaran (2011). Sex, race, and age distributions of mean aortic wall thickness in a multiethnic population-based sample. *Journal of Vascular Surgery* 53(4), 950-957.
- Sakalihan, N., R. Limet and O. D. Defawe (2005). Abdominal aortic aneurysm. *The Lancet* 365(9470), 1577-1589.
- Salman, H. E. and H. C. Yalcin (2020). Advanced blood flow assessment in Zebrafish via experimental digital particle image velocimetry and computational fluid dynamics modeling.

- Micron* 130, 102801.
- Scotti, C. M. and E. A. Finol (2007). Compliant biomechanics of abdominal aortic aneurysms: A fluid–structure interaction study. *Computers & Structures* 85(11-14), 1097-1113.
- Scotti, C. M., J. Jimenez, S. C. Muluk and E. A. Finol (2008). Wall stress and flow dynamics in abdominal aortic aneurysms: finite element analysis vs. fluid–structure interaction. *Computer Methods in Biomechanics and Biomedical Engineering* 11(3), 301-322.
- Shang, E. K., D. P. Nathan, E. Y. Woo, R. M. Fairman, G. J. Wang, R. C. Gorman, J. H. Gorman III and B. M. Jackson (2015). Local wall thickness in finite element models improves prediction of abdominal aortic aneurysm growth. *Journal of Vascular Surgery* 61(1), 217-223.
- Simsek, F. G. and Y. W. Kwon (2015). Investigation of material modeling in fluid–structure interaction analysis of an idealized three-layered abdominal aorta: Aneurysm initiation and fully developed aneurysms. *Journal of Biological Physics* 41(2), 173-201.
- Soudah, E., E. Y. K. Ng, T. H. Loong, M. Bordone, U. Pua and S. Narayanan (2013). CFD modelling of abdominal aortic aneurysm on hemodynamic loads using a realistic geometry with CT. *Computational and Mathematical Methods in Medicine* 2013, 472564.
- Speelman, L., A. Bohra, E. M. H. Bosboom, G. W. H. Schurink, F. N. van de Vosse, M. S. Makaroun and D. A. Vorp (2006). Effects of wall calcifications in patient-specific wall stress analyses of abdominal aortic aneurysms. *Journal of Biomechanical Engineering* 129(1), 105-109.
- Speelman, L., E. M. H. Bosboom, G. W. H. Schurink, F. A. M. V. I. Hellenthal, J. Buth, M. Breeuwer, M. J. Jacobs and F. N. van de Vosse (2008). Patient-specific AAA wall stress analysis: 99-percentile versus peak stress. *European Journal of Vascular and Endovascular Surgery* 36(6), 668-676.
- Sugimoto, K., Y. Takahara, K. Mogi, K. Yamazaki, K. Tsubota, F. Liang and H. Liu (2014). Blood flow dynamic improvement with aneurysm repair detected by a patient-specific model of multiple aortic aneurysms. *Heart and Vessels* 29(3), 404-412.
- Tanweer, O., T. A. Wilson, E. Metaxa, H. A. Riina and H. Meng (2014). A comparative review of the hemodynamics and pathogenesis of cerebral and abdominal aortic aneurysms: Lessons to learn from each other. *Journal of Cerebrovascular and Endovascular Neurosurgery* 16(4), 335-349.
- Thurston, G. B. (1979). Rheological parameters for the viscosity viscoelasticity and thixotropy of blood. *Biorheology* 16(3), 149-162.
- Vande Geest, J. P., M. S. Sacks and D. A. Vorp (2006a). The effects of aneurysm on the biaxial mechanical behavior of human abdominal aorta. *Journal of Biomechanics* 39(7), 1324-1334.
- Vande Geest, J. P., M. S. Sacks and D. A. Vorp (2006b). A planar biaxial constitutive relation for the luminal layer of intra-luminal thrombus in abdominal aortic aneurysms. *Journal of Biomechanics* 39(13), 2347-2354.
- Venkatasubramaniam, A. K., M. J. Fagan, T. Mehta, K. J. Mylankal, B. Ray, G. Kuhan, I. C. Chetter and P. T. McCollum (2004). A comparative study of aortic wall stress using finite element analysis for ruptured and non-ruptured abdominal aortic aneurysms. *European Journal of Vascular and Endovascular Surgery* 28(2), 168-176.
- Vorp, D. A. and J. P. V. Geest (2005). Biomechanical determinants of abdominal aortic aneurysm rupture. *Arteriosclerosis, Thrombosis, and Vascular Biology* 25(8), 1558-1566.
- Vorp, D. A., M. L. Raghavan and M. W. Webster (1998). Mechanical wall stress in abdominal aortic aneurysm: Influence of diameter and asymmetry. *Journal of Vascular Surgery* 27(4), 632-639.
- Wang, X. and X. Li (2013). A fluid-structure interaction-based numerical investigation on the evolution of stress, strength and rupture potential of an abdominal aortic aneurysm. *Computer methods in biomechanics and biomedical engineering* 16(9), 1032-1039.
- Wolters, B. J. B. M., M. C. M. Rutten, G. W. H. Schurink, U. Kose, J. de Hart and F. N. van de Vosse (2005). A patient-specific computational model of fluid–structure interaction in abdominal aortic aneurysms. *Medical Engineering & Physics* 27(10), 871-883.
- Wu, J. and S. C. Shadden (2015). Coupled simulation of hemodynamics and vascular growth and remodeling in a subject-specific geometry. *Annals of Biomedical Engineering* 43(7), 1543-1554.
- Zhang, H., X. Zhang, S. Ji, Y. Guo, G. Ledezma, N. Elabbasi and H. deCougny (2003). Recent development of fluid–structure interaction capabilities in the ADINA system. *Computers & Structures* 81(8-11), 1071-1085.